

Online Research @ Cardiff

This is an Open Access document downloaded from ORCA, Cardiff University's institutional repository: <http://orca.cf.ac.uk/118615/>

This is the author's version of a work that was submitted to / accepted for publication.

Citation for final published version:

Nastase, Stefan Adrian, O'Malley, A. J., Catlow, Charles . R. A. and Logsdail, Andrew J. 2019. Computational QM/MM investigation of the adsorption of MTH active species in H-Y and H-ZSM-5. *Physical Chemistry Chemical Physics* 21 (5) , pp. 2639-2650. 10.1039/C8CP06736H file

Publishers page: <http://dx.doi.org/10.1039/C8CP06736H> <<http://dx.doi.org/10.1039/C8CP06736H>>

Please note:

Changes made as a result of publishing processes such as copy-editing, formatting and page numbers may not be reflected in this version. For the definitive version of this publication, please refer to the published source. You are advised to consult the publisher's version if you wish to cite this paper.

This version is being made available in accordance with publisher policies. See <http://orca.cf.ac.uk/policies.html> for usage policies. Copyright and moral rights for publications made available in ORCA are retained by the copyright holders.



Computational QM/MM investigation of the adsorption of MTH active species in H-Y and H-ZSM-5

S.A.F. Nastase^a, *A.J. O'Malley*^{b,c}, *C.R.A. Catlow*^{a,b,d}, *A.J. Logsdail*^{a,*}

a) Cardiff Catalysis Institute, School of Chemistry, Cardiff University, CF10 3AT, UK

b) UK Catalysis Hub, Research Complex at Harwell, Science and Technology Facilities Council Rutherford Appleton Laboratory, Harwell Science and Innovation Campus, Oxon OX11 0QX, UK

c) Centre for Sustainable Chemical Technologies (CSCT), Department of Chemistry, University of Bath, Bath, BA2 7AY, UK

d) Department of Chemistry, University College of London, 20 Gordon St., London WC1 HOAJ, UK

*) Corresponding Author: LogsdailA@cardiff.ac.uk

KEYWORDS: Methanol-to-Hydrocarbons, methanol zeolites, H-ZSM-5, H-Y, QM/MM

ABSTRACT: The transformation of methanol-to-hydrocarbons (MTH) has significant potential as a route to synthesise low-cost fuels; however, the initial stages of the zeolite catalysed MTH process remain poorly understood. Here, we use hybrid quantum- and molecular-mechanical (QM/MM) embedded-cluster simulations to develop our understanding of the interaction between methanol and the zeolite catalysts H-ZSM-5, and for comparison, the larger pore H-Y. Energies and structures, calculated using hybrid-level density functional theory (hybrid-DFT) and higher-level correlated methods, are compared with previous experimental and computational results. We show that hydrogen-bonds between methanol adsorbates, formed through polarizable O-H bonds, substantially influence the adsorption energetics, structural parameters and vibrational frequencies. Our observations are extended by considering polar

solvent molecules in the environment, with the presence of both water or methanol around the adsorption site leading to barrier-less transfer of the zeolite proton to an adsorbed methanol, which will significantly influence the reactivity of the adsorbed methanol.

1. Introduction

Continued demand for low-cost energy, coupled with decreasing natural fossil fuel reserves, has motivated an intensive scientific search for alternative energy sources to those on which our society has become dependent.¹ Of the various energy sources under current consideration, the synthesis of liquid fuel from coal, biomass and other sources could play a key role in supplying affordable, portable energy in parallel with the uptake of renewable energy technologies.

To make the target hydrocarbons, one can use either the Fischer-Tropsch² or methanol-to-hydrocarbons (MTH) processes^{3,4}. Development of the MTH process was led by Silvestri and Chang at the Mobil Company, whose studies on the methylation of isobutane concluded that the zeolite H-ZSM-5 can catalyse the formation of higher olefins and aromatics.^{5,6,7} These observations initiated sustained industrial and academic investigations of the MTH process in zeolites,^{8,9,10} which identified that the first step is dehydration of the methanol to form framework-bound methoxy- species; subsequently, dimethyl ether (DME), ethene, higher olefins and aromatics are all formed. The nature of the catalytic active site, and the surrounding topology, has been shown to influence significantly the overall reaction, with zeolites like H-ZSM-5 remaining the catalyst of choice in current industrial applications.¹¹

Zeolites, or zeotype catalysts in the form of aluminosilicates or aluminophosphates, have the typical advantages of heterogenous catalysts, such as good mechanical and thermal stability, and facile separation from reaction mixtures.¹² Furthermore, the range of possible framework topologies for zeolites, and the easily tuneable Si:Al composition, ensures flexible reactivity,^{13,14,15,16} however, there remains a

deficit of knowledge at the molecular level as to how the different structural frameworks affect activity and selectivity. For the MTH process, it has been observed that the high reactivity of zeolite catalysts facilitates undesirable side reactions, though these can be suppressed by reducing the acidic character of the zeolite. In particular, weakening the strength or concentration of the acid sites,^{17,18,19} coupled with “directing” the reactions towards the desired products by varying the pore size,^{20,21} can ensure high selectivity. As examples, 10- or 12-membered-ring zeolites, such as H/Na-ZSM-5 (MFI), mordenite (MOR) and H-Beta (BEA), are used for the methanol-to-aromatics process (MTA); one dimensional, large pore zeolites such as ZSM-22 (TON) and ZSM-23 (MTT) are used to obtain C₅₊ aliphatics; and small pore zeolites, such as H-SAPO-34 (CHA) or H-SAPO-18 (AEI), are better for product selectivity in the latter stages of the MTH process as their pore size hinders the diffusion of higher olefins or aromatic compounds.^{11,22} Bjorgsen *et al.* noted that the acidic strength can also determine the functional lifetime of the zeolite catalysts; on comparing the activity of two CHA topology-materials, the silicoaluminophosphate SAPO-34 and the zeolite SSZ-13, both with similar crystallite size and acid site densities but different acid strength, the material with the highest acid strength (H-SSZ-13) yielded more coke and deactivated more quickly.²³ Similar results were observed by Olsbye *et al.* for two zeolite catalysts with similar topologies but different acid site densities (i.e. different acidity); the more acidic ITQ-13 (ITH) and IM-5 (IMF) had higher conversion rates (for butane/butene and C₆₊ aliphatic/aromatic) but deactivated faster than the less acidic ZSM-22 (TON) and ZSM-23 (MTT).¹¹

Recently, O'Malley *et al.* presented strong evidence of a low barrier for formation of methoxy groups on the zeolite framework; quasi- and inelastic neutron scattering data shows that framework methoxylation occurs spontaneously in flow conditions at room temperature in H-ZSM-5 (MFI) but not H-Y (FAU), both with Si/Al ratios of 30.²⁴ The authors suggested that the steam pre-treatment of H-Y, necessary to dealuminate the framework so as to raise heat stability and Brønsted acidity, results in framework silanol and hydroxyl defects that diminish the methoxylation capability compared to H-ZSM-

5. Computational simulations also suggest that the adsorption and methoxylation energetics could be related to the formation of stabilizing hydrogen bonds between the sorbate and framework.²⁵ However, several IR spectroscopy studies indicate apparently contradictory results that the methanol is either protonated to form the methyloxonium ion,²⁶ reducing the energy barrier towards methoxylation,²⁷ or that the methanol is simply physisorbed.^{28,29} Indeed a recent IR study of Matam *et al*³⁰ suggests that both methoxylated and H-bonded species may be present.

To progress understanding of the methanol/zeolite interaction, we present here a computational investigation that aims to clarify the first stages of the MTH process involving adsorption of methanol at the Brønsted acid sites. We highlight the significant role of solvation on CH₃OH adsorption energetics by investigating the co-adsorption of a range of molecules present from either the reaction feed or as reaction by-products.

2. Methodology

2.1 Models

Most previous simulations of zeolites have used discrete clusters^{31,32} or periodic unit cell approaches.^{27, 33} In the former case, the lack of long-range structure or electrostatics, and chemical inaccuracies arising from saturating the cluster's dangling bonds with hydrogen atoms, can alter the accuracy of the calculation outcomes.³² In the latter approach, periodic boundary conditions (PBC) are coupled with a planewave basis set to resolve these issues of bulk representation, but the simulations remain highly computationally demanding for accurate hybrid density functional theory (hybrid-DFT), and higher level correlated approaches, as a full unit cell must be modelled, which can be up to e.g. 288 atoms for H-ZSM-5. Thus, most PBC studies are of small unit cell zeolites such as chabazite (CHA) or sodalite (SOD), or use lower-level GGA-DFT^{27, 33} To overcome these limitations, we use an embedded-cluster hybrid quantum- and molecular-mechanical (QM/MM) method in this current work, as this approach accurately represents both

the local and long-range environment, and offers tractable computing times for accurate hybrid-DFT (and beyond) approaches. Our calculations are performed using the software package “ChemShell”³⁴ with an additive coupling scheme that combines the accuracy of *ab initio* methods, which describes the active site, with the affordability of forcefield models for the long-range periodic electrostatic environment^{35,36}.

To perform the QM/MM calculations, we first create spherical embedded-cluster models of H-ZSM-5 and H-Y from the experimental unit cells of siliceous MFI³⁷ and FAU³⁸, respectively, centred on a Si tetrahedral (T-)site of interest. Whilst FAU has only one symmetry inequivalent T-site, MFI has 12 symmetry inequivalent T-sites. Thus, in order to sample different reaction environments in H-ZSM-5, we have considered 3 different T-sites as focal points for models of this material: the straight channel [T1 (M7)], the sinusoidal channel [T4 (Z6)] and the more open channel intersections [T12 (I2)], as displayed in Figure 1. After creating our embedded-cluster model, we replaced the central Si atom in each model with an Al atom, and have added a charge compensating H on a neighbouring oxygen atom in a manner that facilitates reaction modelling, specifically where the H atom is most accessible, noting that the energy differences between H locations are typically small^{25,39,40}.

The QM region, which is the chemically active part of our model, includes atoms up to the fifth nearest neighbour (the third oxygen atom) from the central T-site (Figure 2A). During QM calculations, the terminal oxygens are saturated with hydrogen atoms: these artificial “link” atoms do not inadvertently affect the electronic solution of the QM calculations, as a bond-dipole correction is added at the boundary to the surrounding MM region, to ensure an accurate electrostatic embedding potential.⁴¹ Encapsulating the QM region are two concentric MM regions, as shown in Figure 2B and 2C. The inner MM region contains atoms that can move during a geometry optimisation; and the outer region is frozen to ensure a

bulk-like structure at the far limit from any chemical reactions. In our calculations, the inner and outer MM regions extend from the central T-site to a radius of 10.58 Å (20 a_0) and 21.17 Å (40 a_0), respectively.

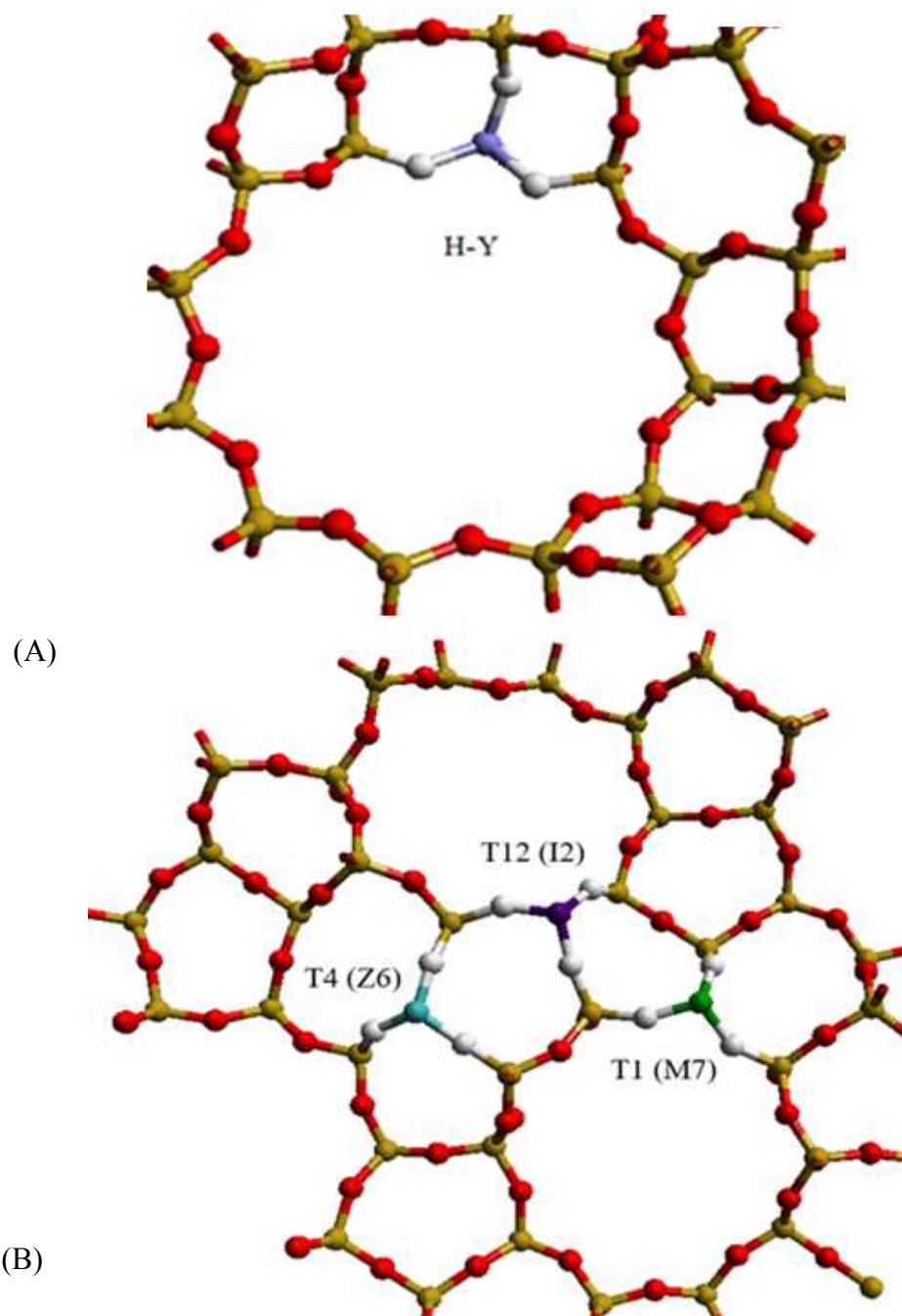


Figure 1. QM/MM embedded cluster models: (a) cutaway view of H-Y active site; (b) cutaway of H-ZSM-5 showing possible active sites. For simulations, only one active site is included in the cluster model. Silicon and oxygen are represented in yellow and red, respectively. The T-site of interest in H-Y is illustrated in grey in (a), and the Z6, I2 and M7 T-sites in H-ZSM-5 are represented in aqua, purple and green, respectively, in (b), with neighbouring O atoms shown in white.

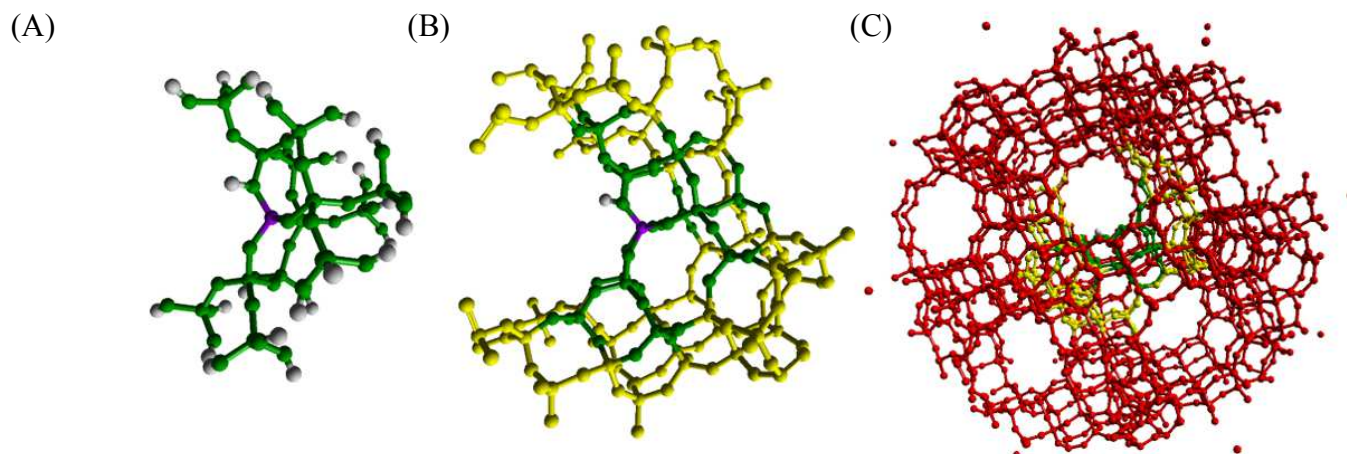


Figure 2. Example of the QM/MM setup in H-Y with regions highlighted being: (A) QM region (green); (B) relaxed MM region (yellow); (C) fixed MM region (red).

Surrounding the entire QM/MM cluster is a series of embedding point charges, the values of which have been fitted to reproduce the bulk electrostatic potential for all the sites allowed to move during any geometry optimisation (*i.e.* the QM and inner MM region), as referenced against a periodic MM calculation for the same system.^{42,43} In their entirety, the total number of atoms in each cluster model is: 1653 for H-Y, with 62 QM atoms and 130 inner MM atoms; 2165 for H-ZSM-5 [T12 (I2)], with 74 QM atoms and 197 inner MM atoms; 2180 for H-ZSM-5 [T1 (M7)], with 67 QM atoms and 207 inner MM atoms; and 2155 for H-ZSM-5 [T4 (Z6)], with 72 QM atoms and 184 inner MM atoms.

Throughout, the QM energy has been calculated using hybrid-DFT with the Becke97-3 exchange-correlation (XC) functional,⁴⁴ as provided in the GAMESS-UK code.⁴⁵ Additional energy calculations, where highlighted, were performed post-geometry optimisation using the dispersion corrected B97-D functional⁴⁶ and higher-level Møller-Plesset perturbation theory (MP2) functionality of NWChem.⁴⁷ This approach was chosen as this work is the foundation for a more extensive investigation of the

thermochemical process of methoxylation, for which B97-3 is an appropriate exchange-correlation functional; comparison of B97-3 and B97-D geometry optimised models showed negligible geometric differences between structures (~ 0.01 Å) and minimal changes to derived energetic results (5 kJ/mol). More details are presented in Table S3 of the SI. Throughout, the atomic orbitals are represented using the Ahlrichs and Taylor TZVP Gaussian basis sets.⁴⁸ The self-consistent field (SCF) convergence criteria was set to an energy change of less than 2.72×10^{-6} eV (1×10^{-7} Hartrees) between SCF iterations.^{49,50} The MM energy was calculated using DL_POLY,⁵¹ employing the forcefield of Hill and Sauer,^{42,43} with the coordination dependent charges in the original forcefield replaced with fixed 1.2 and -0.6 e point charges for silicon and oxygen respectively, as parameterised in the work of Sherwood *et al.*⁴¹ **Because we have a neutrally charged system, we employed Restricted Hartree-Fock (RHF) conditions to simulate our models, corresponding to all spins being paired and singlet spin multiplicity.**

Geometry optimizations were performed by ChemShell in a Cartesian coordinate space using the Limited-Memory Broyden-Fletcher-Goldfarb-Shanno (L-BFGS) algorithm, with a convergence threshold of 0.015 eV/Å, gradients of root-mean-square (rms) of 0.002 Ha/ a_0 , rms of 0.008 a_0 , maximum gradient of 0.003 Ha/ a_0 , maximum displacement of 0.012 a_0 .^{52,53,54,55} Vibrational frequencies were also calculated using ChemShell, with a task-farmed finite-difference approach,⁴⁵ allowing us to compute thermal corrections (i.e. free energies) as well as confirm that geometries correspond to local minima.^{56,57} For the vibrational calculations, only the active site, first neighbour framework atoms, and the adsorbate atoms were displaced; comparison of this approximation against displacement of all atoms in the QM region shows negligible differences [For details see the Supporting Information (SI), Table S1. **No scaling factor has been used to scale our vibrational frequencies, whilst previous work has used a scaling factor to align vibrational frequencies with experiment, with values between 0.9 – 0.9614.**^{58,59,60,61} **In this work no such scaling was pursued due to the absence of necessary benchmarking and derivation in the literature.**

2.2 Energetic analysis

The adsorption energy (E_{ads}) of an adsorbate is calculated as:

$$(1) \quad E_{\text{ads}} = E[\text{ZeOH+Sorbate}] - E[\text{ZeOH}] - E[\text{Sorbate}],$$

where, $E[\text{ZeOH}]$, $E[\text{Sorbate}]$ and $E[\text{ZeOH+Sorbate}]$ are the total energy of the zeolite sorbent, the gas-phase sorbate and the combined guest-host system, respectively, each in their optimised geometry. Due to our use of an atom-centred basis set, it is necessary to include a basis-set-superposition-error (BSSE)⁶² for the combined system, which is calculated thus:

$$(2) \quad E_{\text{BSSE}} = \left(E[\text{ZeOH}_{\text{ads}} + \text{Basis}(\text{Sorbate}_{\text{ads}})] - E[\text{ZeOH}_{\text{ads}}] \right) \\ + \left(E[\text{Sorbate}_{\text{ads}} + \text{Basis}(\text{ZeOH}_{\text{ads}})] - E[\text{Sorbate}_{\text{ads}}] \right),$$

where the first term gives the BSSE (E_{BSSE}) for the framework when including the sorbate orbitals, and the second term gives the E_{BSSE} for the sorbate in the presence of the zeolite orbitals. Thus, in both parts the BSSE is calculated as the difference in energy of the system components (ZeOH and Sorbate) in an adsorbed geometry (denoted with _{ads}), with and without the basis functions (denoted as “Basis”) for the second component of the complete system. e.g. $E(\text{ZeOH})$ is calculated with and without the basis functions of the sorbate present.²⁵ All values of E_{BSSE} are given in the SI (Table S2), and E_{BSSE} is included in all energies reported; generally, the error is ≤ 5 kJ/mol for a single adsorbed CH_3OH .

Additionally, we determined the distortion energy for each adsorbed system, which characterizes the energetic penalty of structural change for the frameworks and sorbates *post-adsorption*. We also calculated the interaction energy between the zeolite and the sorbed molecules *post-adsorption*, which characterizes the strength of the chemical interaction when the sorbate is bound to the framework. These

values allow clarification as to the extent to which the system is strained in order to strengthen E_{ads} . The distortion energy, E_{dist} , is determined for the zeolite as:

$$(3) \quad E_{\text{dist}} = E(\text{ZeOH}_{\text{ads}}) - E(\text{ZeOH})$$

where $E(\text{ZeOH}_{\text{ads}})$ is the SCF energy of the zeolite geometry *after* CH_3OH absorption, i.e. with the CH_3OH removed, and E_{ZeOH} is as defined for Equation (1). A similar approach to Equation (3) exists in the case of CH_3OH , using adsorbed and gas-phase molecular geometries. Subsequently, the interaction energy, E_{int} , is defined as:

$$(4) \quad E_{\text{int}} = E_{\text{ads}} - \sum E_{\text{dist}},$$

with the sum running over E_{dist} for both the zeolite and CH_3OH components.

3. Results and Discussion

3.1 Adsorption of methanol

To test our approach initially, E_{ads} was calculated for CH_3OH in “end-on” and an “side-on” orientations to the zeolite framework (Figure 3). The CH_3OH oxygen is directed towards the acidic site in both cases, but for the “side-on” orientation the reactant is positioned parallel to the pore walls, and for the “end-on” case positioned perpendicular to the walls. Thus, the framework oxygen is coordinated either with the $-\text{CH}_3$, or $-\text{OH}$ group of CH_3OH , respectively.

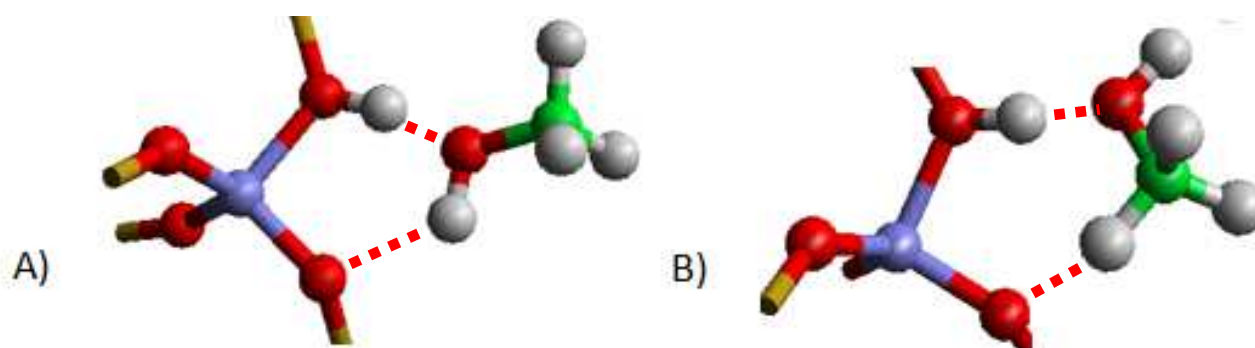


Figure 3. Representation of Single CH_3OH adsorption configurations: A) “end-on” B) “side-on”. Hydrogen-bonds are identified with dotted red lines. Aluminium, hydrogen, carbon and oxygen as shown as purple, white, green and red atoms, respectively.

E_{ads} is exothermic for all systems (Table 1), in the range of -70 to -82 kJ/mol for the “end-on” configuration and -65 to -85 kJ/mol for the “side-on” equivalents for calculations employing the B97-3 functional, with adsorption generally stronger in H-ZSM-5. The results match previous PBC simulations with the PBE exchange-correlation functional⁶³, which report $E_{\text{ads}} = -89$ kJ/mol for the H-ZSM-5 [I2] site. The results also match embedded-cluster calculations by O’Malley et al.,²⁵ who obtained (corrected) adsorption energies of -62 to -69 kJ/mol in H-Y, using PW91, B3LYP and B97-2 exchange-correlation functionals, which are similar to our results. The same authors reported adsorption energies in H-ZSM-5,

with the same functionals, giving results for H-ZSM-5 [I2], [Z6] and [M7] as -50 to -69, -18 to -30, and -84 to -98 kJ/mol respectively. Whilst our I2 and M7 outcomes match this previous work, the difference observed for H-ZSM-5 [Z6] follows from a more comprehensive search in the present work of the energy surface for the adsorbed structure, thus highlighting the general complexity of the potential energy landscape for methanol adsorption. Experimental studies also report E_{ads} as (-90; -110) kJ/mol at 300 K⁶⁴ (with the interval based on the type of Td site the Al occupies), -110 kJ/mol at 323 K⁶⁵ and -115 kJ/mol at 400 K⁶⁶ for H-ZSM-5. It is important to note that differences between experimental and theoretical obtained values, may come from reactant coverage, acid site strength, acid site density^{11,23} and a detailed comparison with experiment would need to include thermal effects and the energies of sorbate-sorbate interactions at higher coverage.

Table 1. Adsorption energy for CH₃OH, presented in kJ/mol.

XC functional:	B97-3		B97-D		MP2	
Site	“End on”	“Side on”	“End on”	“Side on”	“End on”	“Side on”
H-Y	-70	-65	-106	-100	-102	-96
H-ZSM-5 [I2]	-81	-78	-124	-120	-117	-113
H-ZSM-5 [Z6]	-82	-80	-126	-115	-121	-112
H-ZSM-5 [M7]	-81	-85	-115	-114	-107	-113

We note, however, that the B97-3 calculations do not include the effects of dispersion and in order to consider further these effects, we performed additional single point energetic calculations using the B97-3 optimised geometries. E_{ads} was recalculated with the dispersion-corrected version of the B97-3 hybrid-functional, B97-D, as well as an explicitly correlated method in the form of second order Møller-Plesset (MP2) perturbation theory. The dispersion corrections increase the adsorption energies by ~50% (Table 1) and are quantitatively similar to the previously reported PBE-D simulations for single methanol ($E_{\text{ads}} = 115$ kJ/mol),⁶³ and are also much closer to experiment. Generally, the results from these calculations give similar trends to our B97-3 calculations: the H-ZSM-5 active sites promote a higher stability than H-

Y, and the same stability hierarchy is observed for the end-on and side-on configurations. However, we also note small discrepancies between functionals in the adsorption energies of the H-ZSM-5 side-on models, which highlights subtle differences in the energy landscape for each separate approach.

Overall, our results confirm that the “end-on” configuration is marginally more stable for CH₃OH adsorption, matching previous reports^{67,68}, though there is an exception for the H-ZSM-5 [M7] “side-on” model; in this case, geometric analysis shows that the CH₃OH has rotated during optimisation to the “end-on” geometry (Figure 4). Analysis of E_{int} and E_{dist} (SI, Table S4) suggests that the overarching reason for the “end-on” stability is that it distorts the framework less than the “side-on” geometry, as E_{dist} is lower in the former case. Again, this difference can be observed structurally in Figure 4, with the -CH₃ groups only loosely coordinated with the framework for “side-on” orientations. Furthermore, the methyl group (-CH₃) is positioned towards the centre of the zeolite pore for all “end-on” geometries; thus, direct bonding interactions with the framework are fewer in this model, with only direct interactions occurring through the -OH group. Overall, E_{ads} is similar for all sites considered in H-ZSM-5. Comparing adsorption geometries in H-Y and H-ZSM-5, the distance between framework Brønsted sites and -OH groups are consistent throughout, despite notably different adsorption energies for the frameworks, which indicates that additional interactions play a role in the stabilisation of CH₃OH. For further insight about single methanol adsorption on zeolites, we refer the reader to previous work on this field.^{27,31,69,70,71}

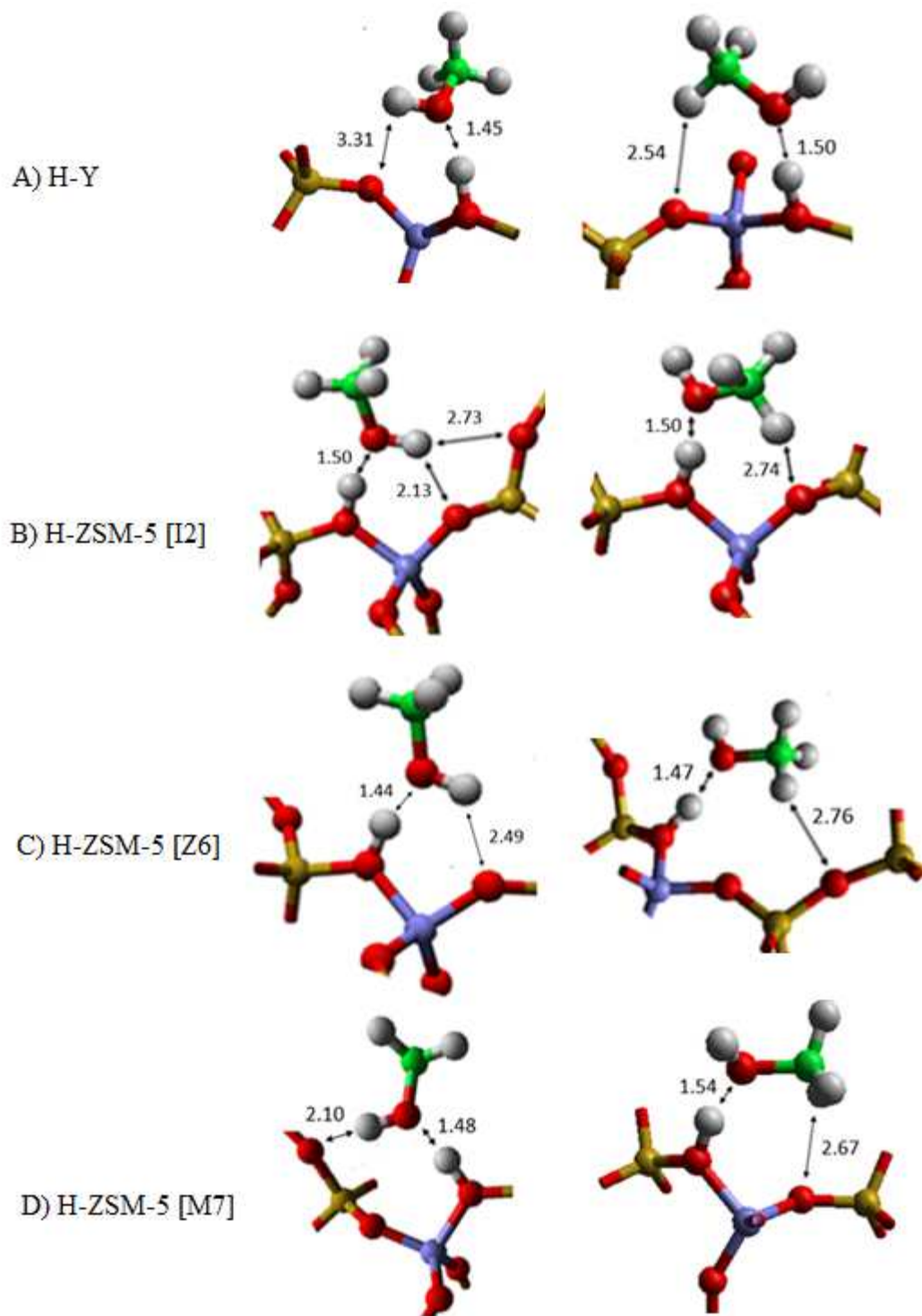


Figure 4. Focused view of zeolite pores showing the B97-3 optimised geometries of CH₃OH adsorbed “end-on” (left) and “side-on” (right) at the zeolite active sites. Hydrogen-oxygen interaction distances are indicated by double-headed arrows (Å). Atoms are coloured as in Figure 3.

Table 2 gives the geometric interactions for the adsorbed methanol with the zeolite framework. Beyond the primary hydrogen bond between the methanol -OH and framework Brønsted site, we have tabulated all additional hydrogen bonds with an interatomic distance below 3 Å. Here, we focus on hydrogen bonds between a framework oxygen and a hydrogen of either the -OH or -CH₃ groups on CH₃OH, irrespective of directionality; greater detail is presented in the SI, Table S5. The most significant stabilising effect is expected from the -OH_{MeOH}···O_{Zeo} interaction, due to the stronger dipole in the -OH moiety (higher acceptor character); however, we also include the -CH_{MeOH}···O_{zeo} interaction in light of theoretical⁷² and experimental⁷³ studies.

Table 2. Details of the primary hydrogen bond length between the methanol oxygen and zeolite H, denoted $d(\text{O}_{\text{MeOH}}\text{-H}_{\text{zeo}})$, and number of secondary hydrogen-type bonding interactions between the -OH and -CH₃ molecular fragments of the CH₃OH and the zeolite framework. The length of the primary hydrogen bond is given in Å.

	“Side-on”			“End-on”		
	$d(\text{O}_{\text{MeOH}}\text{-H}_{\text{zeo}})$	<i>H-bonds</i>		$d(\text{O}_{\text{MeOH}}\text{-H}_{\text{zeo}})$	<i>H-bonds</i>	
		-OH	-CH ₃		-OH	-CH ₃
H-Y	1.50	-	2	1.45	2	-
H-ZSM-5 [I2]	1.50	-	1	1.50	2	1
H-ZSM-5 [Z6]	1.44	2	3	1.47	2	-
H-ZSM-5 [M7]	1.48	-	1	1.57	2	-

Table 2 suggests that the secondary hydrogen bonds, additional to the primary interaction between O_{MeOH} and H_{zeo}, can influence E_{ads}. In particular, E_{ads} is marginally stronger for “end-on” models where the quantity of shorter secondary interactions is high. For “side-on”, the tight pore active sites of H-ZSM-5 [Z6] and H-ZSM-5 [M7] have caused the methanol to rotate so that the -OH group of the methanol is in fact closer to the framework than the -CH₃ group (Figure 4), which indicates that directionality in the -OH bond is important.

3.2 Bi-methanol systems

Previous work studying the FER framework, has shown that including additional CH₃OH at the adsorption site may result in spontaneous methanol protonation, subsequently lowering the energy barrier for methoxylation.²⁷ Following this observation, we now consider the role of additional neighbouring molecules in our H-Y and H-ZSM-5 models. Firstly, we have considered a second CH₃OH, and have constructed three different bi-methanol configurations (Figure 5).

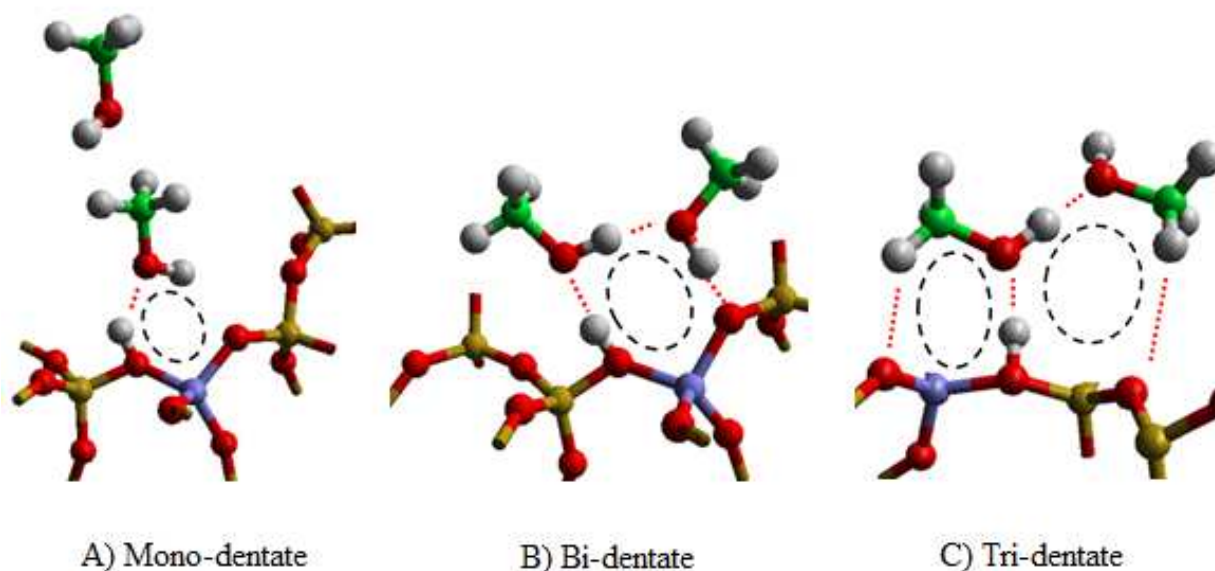


Figure 5. Models of bi-methanol configurations considered in this work: A) mono-dentate, B) bi-dentate, C) tri-dentate. As for Figure 4, hydrogen bonds are marked with dotted red lines and coordination-rings are represented by dashed circles. Atom colours are as for Figure 3.

Fig. 5A) shows the “mono-dentate” configuration, which is considered the most direct pathway to the formation of DME³³. In this model, the “end-on” structure interacts with a second methanol molecule through its -CH₃ group; thus, the CH₃OH coordination with the framework can be directly compared to the adsorption of the single “end-on” molecule (Section 3.1). Two further bi-methanol configurations were considered: an extended 8-membered coordination ring, denoted as

“bi-dentate” (Fig. 5B), or two coordination rings formed by the “side-on” methanol molecules and the zeolite framework, which we term “tri-dentate” (Fig. 5C). As for the single methanol adsorption, we first performed geometry optimisations using the hybrid B97-3 exchange-correlation functional before also performing single point calculations using B97-D and MP2 approaches, with the results presented in Table 3. The dispersion-corrected approaches gave E_{ads} as ~50% more negative; however, though there are some subtle variations in the energetic ordering for adsorption sites, the overall trends of the B97-3, B97-D and MP2 results are similar, detailed discussion of which is presented in the following sub-sections.

Table 3. Calculated adsorption energies when using density functional theory with B97-3, B97-D exchange-correlation functionals, or higher-level MP2 simulations (kJ/mol). The adsorption energy of the secondary CH₃OH, i.e. energy change relative to the single, end-on adsorbed CH₃OH, is given in parentheses.

	B97-3			
	H-Y	H-ZSM-5		
		[I2]	[Z6]	[M7]
Mono-dentate	-90 (-20)	-98 (-17)	-94 (-12)	-82 (-1)
Bi-dentate	-146 (-76)	-142 (-61)	-126 (-44)	-125 (-44)
Tri-dentate	-128 (-58)	-141 (-60)	-126 (-44)	-129 (-48)
	B97-D			
Mono-dentate	-139 (-33)	-160 (-36)	-144 (-18)	-119 (-4)
Bi-dentate	-219 (-113)	-218 (-94)	-196 (-70)	-197 (-82)
Tri-dentate	-199 (-93)	-223 (-99)	-185 (-59)	-189 (-74)
	MP2			
Mono-dentate	-133 (-31)	-180 (-63)	-141 (-20)	-113 (-6)
Bi-dentate	-211 (-109)	-206 (-89)	-191 (-70)	-190 (-83)
Tri-dentate	-192 (-90)	-216 (-99)	-180 (-59)	-180 (-73)

3.2.1. Mono-dentate methanol adsorption

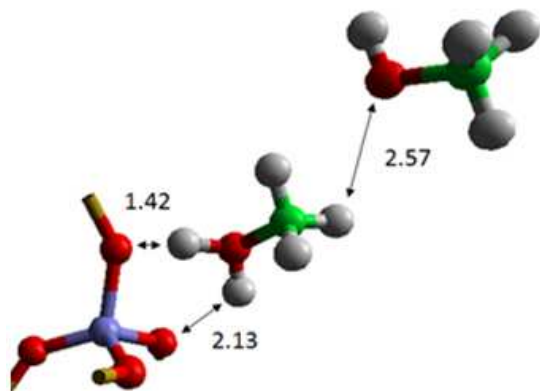
E_{ads} for the mono-dentate models are given in Table 4. Structural analysis shows that the methanol molecule undergoes spontaneous protonation in the two more “open” models (H-Y and H-ZSM-5 [12]), where the framework Brønsted acid has transferred to the primary CH_3OH . Experimental studies detected the presence of the H-O-H^+ signal, **not only when having a dimer²⁶ or trimer^{74,75} adsorbed on the active site, but also when a single methanol^{74,76,77} is adsorbed.**

We propose that the proton transfer occurs because the additional CH_3OH interacts with the $-\text{CH}_3$ group of the framework adsorbed CH_3OH , which then diminishes induction effects on the oxygen of this framework bound CH_3OH .

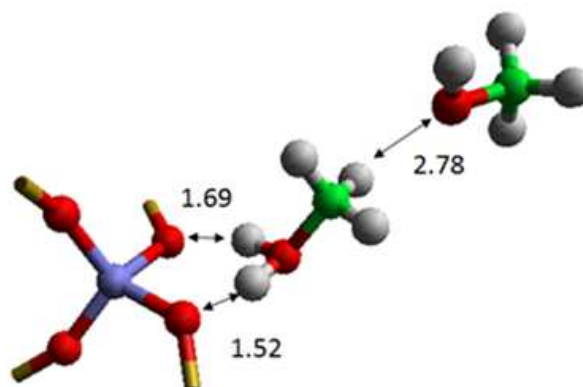
Figure 6 shows the geometries for the mono-dentate systems, with E_{ads} and $-\text{OH}\cdots\text{O}$ interaction distances documented in Table 4. For H-Y, E_{ads} is -90 kJ/mol, which is stronger than the -70 kJ/mol observed for the single CH_3OH . Despite a higher number of $-\text{OH}_{\text{MeOH}}\cdots\text{O}_{\text{zeo}}$ interactions in H-ZSM-5 (with detailed geometric values given in SI, table S5 and S6), E_{ads} is similar both when a methyloxonium ion is formed and when the proton remains bound to the framework, from which we conclude that the electrostatic interactions between the zeolite proton (H_{zeo}) and the hydroxyl group of the methanol ($-\text{OH}_{\text{MeOH}}$) are important in stabilizing the bi-methanol structure (Partial charges on each atom are presented in SI, table S7)

Table 4. Summary of adsorption energies (E_{ads}) and geometric parameters (distances, d) for the most stable bi-methanol adsorption in zeolites H-Y and H-ZSM-5. For the geometric characterisation, “short” hydrogen-bonds of the adsorbed bi-methanol structures are given: ‘H1’ and ‘H2’ are the quantity of hydrogen-bonds formed by the -OH groups on the primary and second CH₃OH, respectively, whilst ‘HC1’ and ‘HC2’ represent the hydrogen bonds formed from the -CH₃ groups of each respective molecule to the zeolite framework. Where appropriate, the parent structure of the atoms, either zeolite (zeo) or methanol (MeOH) is given in subscript after the atomic label. Geometric observables are presented in Å, and E_{ads} in kJ/mol, with the results displayed in bold corresponding to the cases where spontaneous proton transfer occurred.

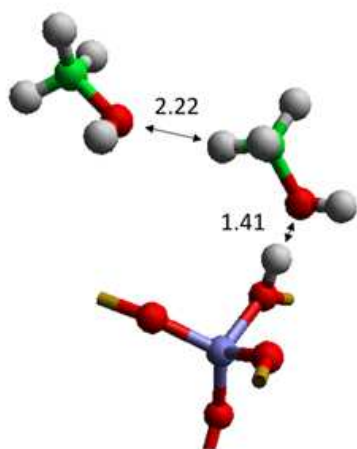
Site	E_{ads} (B97-3)	$d(\text{H}_{\text{zeo}}-\text{O}_{\text{zeo}})$	$d(\text{H}_{\text{MeOH1}}-\text{O}_{\text{MeOH2}})$	H1	H2	HC1	HC2
<i>Mono-dentate</i>							
H-Y	-90	1.42	2.57	1	-	-	-
H-ZSM-5 [I2]	-98	1.69	2.78	2	1	-	2
H-ZSM-5 [Z6]	-94	1.05	2.34	1	2	1	1
H-ZSM-5 [M7]	-82	1.04	2.22	1	-	2	2
<i>Bi-dentate</i>							
H-Y	-146	1.82	1.33	1	2	-	2
H-ZSM-5 [I2]	-142	1.67	1.45	1	2	1	3
H-ZSM-5 [Z6]	-126	1.52	1.55	-	2	1	7
H-ZSM-5 [M7]	-125	1.67	1.40	-	2	2	2
<i>Tri-dentate</i>							
H-Y	-128	1.73	1.51	-	-	2	1
H-ZSM-5 [I2]	-141	1.53	1.50	-	3	2	4
H-ZSM-5 [Z6]	-126	1.60	1.49	-	2	3	-
H-ZSM-5 [M7]	-129	1.49	1.52	-	2	2	4



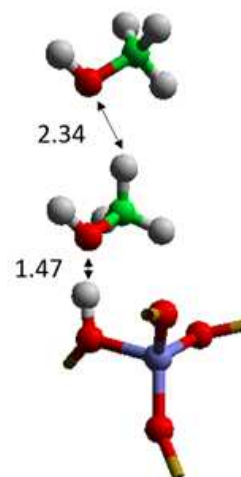
A) H-Y



B) H-ZSM-5 [I2]



C) H-ZSM-5 [Z6]



D) H-ZSM-5 [M7]

Figure 6. Adsorbed B97-3 optimised geometries of mono-dentate bi-methanol in H-Y and H-ZSM-5. Hydrogen-bond distances are marked by arrows, with values given in Å. The atom colours are as in Figure 3.

3.2.2 Bi-dentate methanol adsorption

As shown in Table 4, the ordering of E_{ads} for the bi-dentate adsorption (from strongest to weakest) is $\text{H-Y} > \text{H-ZSM-5 [I2]} > \text{H-ZSM-5 [M7]} > \text{H-ZSM-5 [Z6]}$. A correlation is observed between E_{ads} and the size of the local space around the zeolite active site: H-ZSM-5 channel sites (M7 and Z6) are smaller, and so bonding of the two methanol molecules is weaker, whereas the larger open cages of H-Y and H-ZSM-5 [I2] do not have similar steric limitations. The bi-dentate configurations with highest stability also have a more pronounced proton transfer, shown by the longer $d(\text{H}_{\text{zeo}}-\text{O}_{\text{zeo}})$ in Table 4 and Figure 7. In general, proton transfer occurs more readily when the two methanol molecules are closer together, as is shown by the correlation evident in Figure 8. This trend is further highlighted by the charge transfer on to the hydrogen atoms of the methyloxonium H-O-H, which is higher in the bi-dentate configuration compared to the mono- and tri-dentate cases (Table S7 of SI), which may be an indication as to why the MTH process occurs faster at higher reactant loading^{78,79} and also suggest a possible first step of this reaction, as we will discuss later in our analysis. Furthermore, the most stable adsorbed structures (H-ZSM-5 [I2], H-Y, $E_{\text{ads}} \sim 145$ kJ/mol) have more additional hydrogen bonds than the least stable (H-ZSM-5 [M7], H-ZSM-5 [Z6]), with the $\text{OH} \cdots \text{O}$ interactions between molecules and framework clearly influential.

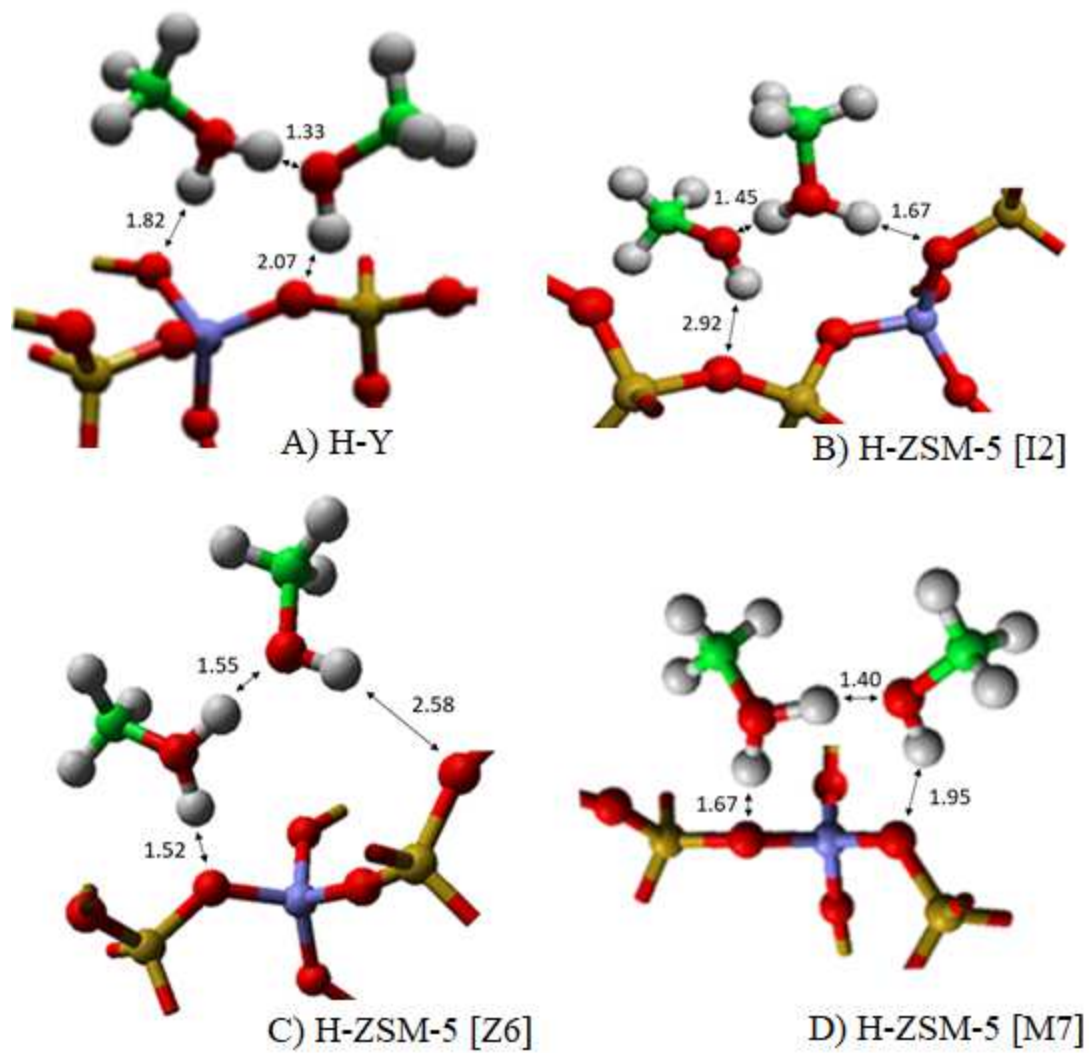


Figure 7. Adsorbed B97-3 optimised bi-dentate geometries in zeolite H-Y and H-ZSM-5. Colour scheme is as for Figure 3. All distances are marked with arrows and given in Å.

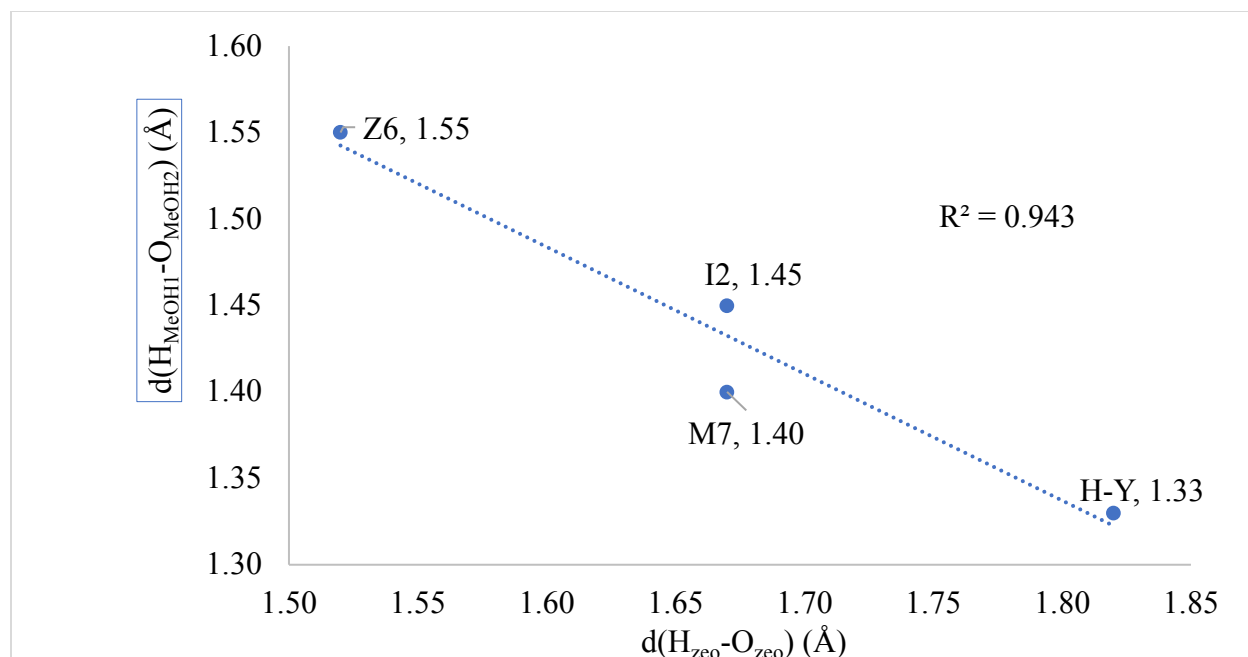


Figure 8. Distance, d , between framework oxygen and protons ($\text{H}_{\text{zeo}}-\text{O}_{\text{zeo}}$) plotted against distance between the two methanol molecules ($\text{H}_{\text{MeOH1}}-\text{O}_{\text{MeOH2}}$) in the bi-dentate configuration (Å). The dotted line is given to guide the eye, with an R^2 given to quantify error in the fit.

3.2.3. Tri-dentate methanol adsorption

The adsorption energies for the tri-dentate arrangements are comparable to those of the bi-dentate (Table 4), with the most stable tri-dentate configuration (displayed in SI, Figure S2) observed in the H-ZSM-5 [I2] structure (-141 kJ/mol). All other frameworks give E_{ads} of -126 to -129 kJ/mol. As with the bi-dentate adsorption, spontaneous proton transfer is observed for the tri-dentate adsorption, resulting in the formation of a methyloxonium ion; however, the hydrogen bonds are slightly different with $d(\text{O}_{\text{zeo}}-\text{H}_{\text{zeo}}) \sim 0.1$ Å shorter than in the bi-dentate structures. More hydrogen bonds are formed in H-ZSM-5 zeolites than H-Y, due to the smaller size of the H-ZSM-5 channel sites.

3.3 Adsorption of methanol in presence of alternative molecular species

Thus far, we have focussed primarily on how the geometry and interactions between CH₃OH molecules around the active site affects E_{ads}. However, other reactants and/or products may be in the reaction stream, and E_{ads} can be affected by their presence. For instance, H₂O, which is a product of framework methoxylation, can form hydrogen bonds with the -OH groups of CH₃OH, which will not be possible with CH₄, a possible feed impurity. We therefore test both H₂O and CH₄ as secondary environmental molecules, which allows us further to compare and contrast the hydrogen-bonding effects on adsorption energies. Building on our models of a single CH₃OH adsorbed at the Brønsted site, various configurations were considered for H₂O (mono and bi-dentate; displayed in Figures S3 and S4 of the SI) and CH₄ (bi-dentate; Figure 9), with all new structures geometry optimised with the B97-3 functional. As before, outcomes were compared to dispersion-corrected B97-D exchange-correlation functional and MP2 approaches to obtain perspective on how long-distance interactions affect the energetics reported.

Table 5. The adsorption energies of the CH₃OH and second species, H₂O or CH₄, with the adsorption energy of just the second molecule (relative to a single, end-on adsorbed CH₃OH) given in parenthesis (kJ/mol), with the results presented in bold corresponding to the cases where spontaneous proton transfer occurs.

Model	H-Y	H-ZSM-5 [I2]	H-ZSM-5 [Z6]	H-ZSM-5 [M7]
B97-3				
H ₂ O Mono-dentate	-90 (-25)	-84 (-3)	-133 (-51)	-123 (-42)
H ₂ O Bi-dentate	-134 (-64)	-134 (-53)	-148 (-66)	-126 (-45)
CH ₄ Bi-dentate	-70 (0)	-70 (11)	-72 (9)	-91 (-10)
B97-D				
H ₂ O Mono-dentate	-140 (-34)	-139 (-15)	-185 (-59)	-175 (-60)
H ₂ O Bi-dentate	-189 (-83)	-206 (-82)	-202 (-76)	-181 (-66)
CH ₄ Bi-dentate	-112 (-6)	-126 (-2)	-123 (3)	-148 (-33)
MP2				
H ₂ O Mono-dentate	-138 (-36)	-129 (-12)	-185 (-64)	-170 (-63)
H ₂ O Bi-dentate	-185 (-83)	-197 (-80)	-198 (-77)	-173 (-66)
CH ₄ Bi-dentate	-104 (-2)	-118 (-1)	-118 (3)	-146 (-39)

E_{ads} for CH₃OH/H₂O and CH₃OH/CH₄ co-adsorption in the 4 different systems is presented in Table 5; as the dispersion-corrected approaches give similar trends to the B97-3 calculated adsorption energies, only the latter is discussed in detail. For H₂O, the strongest adsorption in the mono-dentate configuration is for the more confined H-ZSM-5 [Z6] and H-ZSM-5 [M7] sites; for the bi-dentate, H-ZSM-5 [Z6] is also the most stable adsorption site. This is contrary to CH₃OH co-adsorption, where the more open H-Y and H-ZSM-5 [I2] sites are more stable, and thus indicates steric and/or electronic effects differ in the pores for these different molecular species. Overall adsorption energies are comparable to the bi-methanol adsorption and, also as with the bi-methanol systems, the framework proton on H-ZSM-5 transfers spontaneously to CH₃OH in the presence of H₂O. This proton transfer is also observed for the bi-dentate complex in H-Y, but not

the mono-dentate structure. For CH₄ in the neighbouring environment (i.e. CH₃OH/CH₄), the change in E_{ads} relative to the single methanol is negligible. Energy differences range only from 9 to -6 kJ/mol for the B97-3 exchange-correlation functional; furthermore, no proton transfer occurs, illustrating the importance of hydrogen-bonding from a polarizable -OH group in order to facilitate proton transfer and strong adsorption.

When analysing the geometry of the adsorbed structures, proton transfer from the framework to the CH₃OH generally correlates with higher E_{ads} for CH₃OH/H₂O (detailed in the SI, table S9 and S10), with the exception of the mono-dentate H-Y. For the mono- and bi-dentate CH₃OH/H₂O H-ZSM-5 models, proton transfer from the framework to methanol again correlates with the proximity of the two reactants (SI, Graph S1). From this observation, we suggest that the pore curvature influences the H₂O positioning close to the CH₃OH or the active site, with the former resulting in proton transfer to the CH₃OH.

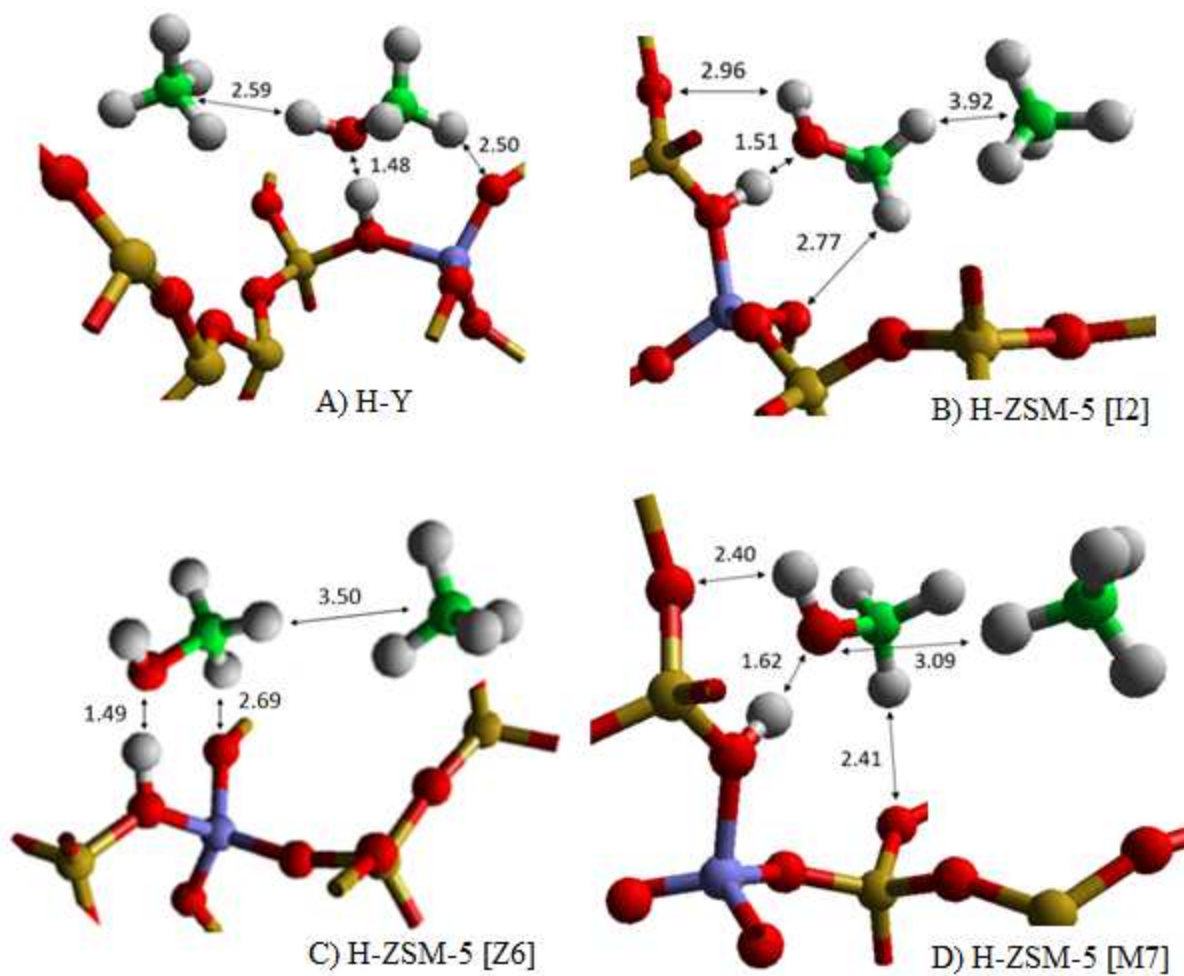


Figure 9. The B97-3 optimised geometries of the CH₃OH and CH₄ models in zeolite pores, with interatomic distances given in Ångstroms. The atom colours are as in Figure 3.

4. Vibrational analysis of adsorbed methanol

In order to understand further the interactions between sorbates and the zeolite framework, and to allow comparison with experiment, vibrational frequency calculations were performed using the geometries obtained with the B97-3 exchange-correlation functional and a finite-difference harmonic approximation approach. The results, presented in Table 6, show that the vibrational frequency of the $O_{zeo}-H_{zeo}$ stretch mode decreases from 3706 cm^{-1} for the empty framework to $2244\text{ (}2498\text{) cm}^{-1}$ when the CH_3OH is adsorbed “end-on” (side-on) in the H-Y framework. This redshift is indicative of weaker bonding of the O-H Brønsted site, i.e. the framework proton is not bound as strongly, and even less so upon adsorbing methanol in the “end-on” configuration. Comparing the vibrational frequencies for the “end-on” and “side-on” models, there is a difference of $\sim 150\text{ cm}^{-1}$ for H-Y, which relates to stronger framework-methanol interactions in the former. This difference between “end-on” and “side-on” is also observed for H-ZSM-5 with the exception of H-ZSM-5 [M7], where the “end-on” vibrational frequencies are higher than “side-on”; which has been highlighted and discussed in Section 3.1, with the “side on” methanol noted as rotating to “end on”. Throughout, the vibrational frequency of the OH bond of the CH_3OH remains constant at $\sim 3900\text{ cm}^{-1}$.

Table 6. Vibrational frequencies of O-H bonds in H-Y, H-ZSM-5 and CH₃OH (cm⁻¹) when considering adsorption of one and two methanol species at the active site. The parent structure of the identified atoms is given in subscript after the atomic label as either zeolite (zeo) or methanol (MeOH).

	H-Y	H-ZSM-5		
		[I2]	[Z6]	[M7]
	O _{zeo} -H _{zeo}			
Empty zeolite	3789	3836	3805	3873
<i>Experiment</i> ²⁶ (in presence of CH ₃ OH)	2440			
<i>Simulations</i> ^{80,58} (in presence of CH ₃ OH)	2548-3235			
Side-on	2498	2581	2504	2725
End-on	2244	2504	2331	2803
	H _{zeo} -O _{MeOH} -H _{MeOH} bending			
<i>Experiment</i> ^{81,82,76}	1600-1800			
<i>Simulations</i> ^{58,83,70}	1635-1687			
Mono-dentate	1778	1734	*	*
Bi-dentate	1736	1799	1803	1847
Tri-dentate	1786	1764	1721	1802
	Asymmetric H _{zeo} -O _{MeOH} -H _{MeOH} stretch			
<i>Experiment</i> ^{81,82,76}	2400-2600			
<i>Simulations</i> ^{58,83,70}	2023-2548			
Mono-dentate	2143	2718	*	*
Bi-dentate	1848	2376	2624	2183
Tri-dentate	2635	2685	2632	2509
	Symmetric H _{zeo} -O _{MeOH} -H _{MeOH} stretch			
<i>Experiment</i> ^{81,82,76}	2700-3100			
<i>Simulations</i> ^{58,83,70}	2549-2900			
Mono-dentate	3039	3037	*	*
Bi-dentate	3098	3082	2786	3078
Tri-dentate	2822	2841	2829	3086

* Values not reported as methyloxonium ion is not formed in these models

Agreement with previous experiment and computational work is established not only in the case of a single CH_3OH adsorption^{26,51} but also for the bi-methanol models; additional vibrational motions appear when adding the second CH_3OH , which is attributed to a protonated CH_3OH . Specifically, the resulting H-O-H bending (or scissoring) and the symmetric and asymmetric O-H stretches of the H-O-H^+ group vibrational modes, with the movements displayed in Figure 10.

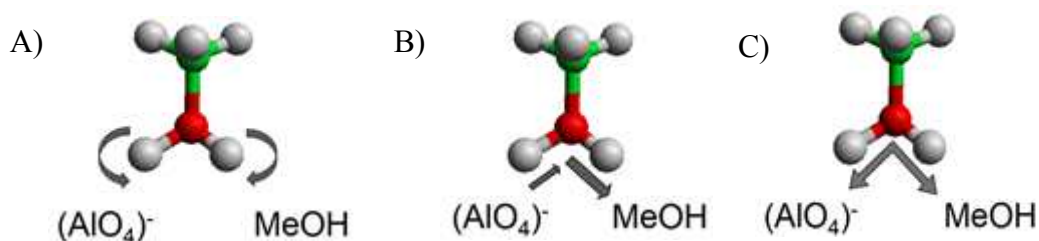


Figure 10. Vibrational modes of the H-O-H group of the methyloxonium molecule, specifically A) H-O-H bending, B) O-H asymmetric stretch, C) O-H symmetric stretch. Atom movements are indicated with grey arrows.

The H-O-H^+ bending motion depends simultaneously on the interaction between the zeolite framework and the co-adsorbed methanol molecule, both mono- and bi-dentate CH_3OH configurations give vibrational frequencies that decrease with increasing adsorption strength (SI, Graph S2). The proximity to the zeolite framework and second methanol molecule also is seen to dictate shifts in the asymmetric and symmetric O-H stretches. In particular, the O-H asymmetric stretch depends inversely on how close the methyloxonium is to the second CH_3OH ; and the O-H symmetric stretch depends on the distance between the zeolite framework and the $-\text{OH}^+$ moiety of the CH_3OH_2^+ , with greater distance leading to lower frequencies (SI, Graph S3 and S4).

The behaviour outlined for the vibrational frequencies of the asymmetric and symmetric O-H stretch were also observed experimentally⁷⁶, with an increase in methanol feed leading to an increase and decrease in their respective signature frequencies. These shifts we suggest correspond to the methyloxonium being part of a bigger and more stable methanol cluster, which would need

to be positioned either in larger pores, or outside of the zeolite framework, due to the requirement of a greater number of methanol-methanol interactions. As highlighted by our results, the changes in the stretching vibrational frequencies can be attributed to the bi-dentate models, which we postulate is indicative that the bi-dentate configuration is observed in the previously mentioned experimental study. Furthermore, in the case of the CH₃ vibrational frequencies, no significant difference is observed between the single and bi-methanol models or between each of the mono, bi or tri-dentate calculations we have performed. Values range from 3076-3276 cm⁻¹ in the single methanol adsorbed models and 3066-3349 cm⁻¹ in the bi-methanol cases, which is in agreement with other experimental⁷⁶ and theoretical studies⁸⁴. This result indicates that the CH₃ moiety is unperturbed during framework interactions, though more work is necessary to correlate further any outcomes from framework methoxylation with changes in vibrational frequencies.

We also analysed the relationship between several electronic parameters (such as band gap, electronegativity, chemical potential and chemical hardness) of the empty zeolite clusters and the adsorption energy or distance between the zeolite framework and Brønsted proton of the single and bi-methanol models and found no correlation. Further details of the methodology and results are given in the “Electronic Parameters Analysis” section of SI.

5. Summary and Conclusions

Species relevant to the methanol to hydrocarbons (MTH) process, as represented by methanol, water and methane, have been studied interacting with zeolite catalysts H-Y and H-ZSM-5 using a hybrid QM/MM approach. The H-ZSM-5 framework stabilizes a single methanol in either a “side-on” or “end-on” geometry, with channels (M7, Z6) preferable over the open intersection sites (I2) and the alternative H-Y framework. For bi-methanol models, the more open H-Y and H-ZSM-5 intersection (I2) have a local-environment that facilitates the stabilization of multiple molecules, when compared to channels. Bi-methanol adsorption was considered in mono-, bi- and tri-dentate arrangements, with the hydroxyl ring formed by a “bi-dentate” configuration being most stable. Polarising hydrogen bonds formed between the -OH groups of the molecules, have a more significant influence on the adsorption energetics than the less polarising hydrogen bonds formed through -CH₃ moieties. The orientation and polarity of molecules at the active site are suggested as being a driving force for spontaneous proton transfer from the framework onto an adsorbed methanol, as justified by spontaneous proton transfer occurring in our calculations with multiple methanol molecules and when water is introduced, but not when methane is introduced. Vibrational frequency calculations allow us to clarify further that the methyloxonium (CH₃OH₂⁺), as formed via a bi-dentate adsorption complex, is also present in previous experiment and thus forms a key component of the initiation of the MTH process. Further work will aim to understand the transformation of the methyloxonium into extended, neutral intermediates such as dimethylether.

Author Contributions

The investigation plan was derived by all authors, and the calculations performed by Stefan Adrian F. Nastase. The manuscript was written through contributions of all authors, and all authors have given approval to the final version of the manuscript.

Acknowledgement

Computing facilities for this work were provided by ARCCA at Cardiff University, Supercomputing Wales, and through our membership of the UK's HPC Materials Chemistry Consortium (MCC), which is funded by the EPSRC (EP/L000202). AJOM would like to acknowledge the Ramsay Memorial trust for provision of a Ramsay Fellowship, and Roger and Sue Whorrod for the funding of the Whorrod Fellowship. Stefan Nastase wishes to thank the School of Chemistry, Cardiff University for a studentship.

Supporting Information:

Additional computational details are provided, specifically: energetic parameters such as variation of vibrational frequencies with size of relaxed region (Table S1) or BSSE values (Table S2) and geometric features in the form of bond lengths, figures and plots displaying or exploring correlations with set bond lengths (Tables S3-7, S9-10, Graphs S1-4 and Figures S1-S4), partial charges of bi-methanol models (Table S8).

References:

- (1) Finn, J.; Nielsen, P. E. H.; Sørensen, P. M. D. *Biomass Convers. Biorefinery* **2011**, *1* (2), 85–90.
- (2) Dry, M. E. *Catal. Today* **2002**, *71* (3–4), 227–241.
- (3) Barthos, R.; Bánsági, T.; Süli Zakar, T.; Solymosi, F. *J. Catal.* **2007**, *247* (2), 368–378.
- (4) Dahl, I.; Kolboe, S. *J. Catal.* **1994**, *149*, 458–464.
- (5) Chang, C. D.; Silvestri, A. J. *J. Catal.* **1977**, *47* (2), 249–259.
- (6) Ghorbanpour, A.; Rimer, J. D.; Grabow, L. C. *ACS Catal.* **2016**, *6* (4), 2287–2298.
- (7) Lesthaeghe, D.; VanderMynsbrugge, J.; Vandichel, M.; Waroquier, M.; VanSpeybroeck, V. *ChemCatChem* **2011**, *3* (1), 208–212.
- (8) Avidan, A. A. *Stud. Surf. Sci. Catal.* **1988**, *36* (C), 307–323.
- (9) Wu, X.; Xu, S.; Zhang, W.; Huang, J.; Li, J.; Yu, B.; Wei, Y.; Liu, Z. *Angew. Chemie - Int. Ed.* **2017**, *56* (31), 9039–9043.
- (10) Liu, Y.; Müller, S.; Berger, D.; Jelic, J.; Reuter, K.; Tonigold, M.; Sanchez-Sanchez, M.; Lercher, J. A. *Angew. Chemie - Int. Ed.* **2016**, *55* (19), 5723–5726.
- (11) Etemadi, S.; Olsbye, U. In *Master's Thesis - Catalytic investigations of zeolite based methanol to hydrocarbons catalysts*; 2015; pp 75–122.
- (12) Wang, P.; Shen, B.; Gao, J. *Catal. Today* **2007**, *125* (3–4), 155–162.
- (13) Colella, C.; Wise, W. S. *Microporous Mesoporous Mater.* **2014**, *189*, 4–10.
- (14) VanSpeybroeck, V.; Hemelsoet, K.; DeWispelaere, K.; Qian, Q.; VanderMynsbrugge, J.;

- DeSterck, B.; Weckhuysen, B. M.; Waroquier, M. *ChemCatChem* **2013**, *5* (1), 173–184.
- (15) Hemelsoet, K.; Van Der Mynsbrugge, J.; De Wispelaere, K.; Waroquier, M.; Van Speybroeck, V. *ChemPhysChem* **2013**, *14* (8), 1526–1545.
- (16) Wang, C. M.; Brogaard, R. Y.; Xie, Z. K.; Studt, F. *Catal. Sci. Technol.* **2015**, *5* (5), 2814–2820.
- (17) Greatbanks, S. P.; Hillier, I. H.; Burton, N. A.; Sherwood, P. J. *Chem. Phys.* **1996**, *105* (9), 3770–3776.
- (18) Wang, C. M.; Brogaard, R. Y.; Weckhuysen, B. M.; Nørskov, J. K.; Studt, F. *J. Phys. Chem. Lett.* **2014**, *5* (9), 1516–1521.
- (19) Brogaard, R. Y.; Wang, C.; Studt, F. *ACS Catal.* **2014**, *4* (12), 4504–4509.
- (20) Fu, H.; Song, W.; Haw, J. F. *Catal. Letters* **2001**, *76* (1–2), 89–94.
- (21) Wang, S.; Wei, Z.; Chen, Y.; Qin, Z.; Ma, H.; Dong, M.; Fan, W.; Wang, J. *ACS Catal.* **2015**, *5* (2), 1131–1144.
- (22) Wang, W.; Jiang, Y.; Hunger, M. *Catal. Today* **2006**, *113* (1–2), 102–114.
- (23) Olsbye, U.; Svelle, S.; Bjrgen, M.; Beato, P.; Janssens, T. V. W.; Joensen, F.; Bordiga, S.; Lillerud, K. P. *Angew. Chemie - Int. Ed.* **2012**, *51* (24), 5810–5831.
- (24) O’Malley, A. J.; Parker, S. F.; Chutia, A.; Farrow, M. R.; Silverwood, I. P.; García-Sakai, V.; Catlow, C. R. A. *Chem. Commun.* **2016**, *52* (14), 2897–2900.
- (25) O’Malley, A. J.; Logsdail, A. J.; Sokol, A. A.; Catlow, C. R. A. *Faraday Discuss.* **2016**,

188 (February), 235–255.

- (26) Mirth, G.; Lercher, J. A.; Anderson, M. W.; Klinowski, J. *J. Chem. Soc. Faraday Trans.* **1990**, 86 (17), 3039.
- (27) Govind, N.; Andzelm, J.; Reindel, K.; Fitzgerald, G. **2002**, 423–434.
- (28) Suwardiyanto, S.; Howe, R. F.; Gibson, E. K.; Catlow, C. R. A.; Hameed, A.; McGregor, J.; Collier, P.; Parker, S. F.; Lennon, D. *Faraday Discuss.* **2017**, 197, 447–471.
- (29) Campbell, S. M.; Jiang, X. Z.; Howe, R. F. *Microporous Mesoporous Mater.* **1999**, 29 (1–2), 91–108.
- (30) Matam, S. K.; Howe, R. F.; Thetford, A.; Catlow, R. C. A. *Chem. Commun.* **2018**.
- (31) Gale, J. D.; Catlow, C. R. a.; Carruthers, J. R. *Chem. Phys. Lett.* **1993**, 216 (1), 155–161.
- (32) Catlow, C. R. A.; Smit, B.; van Santen, R. A. *Computer modelling of microporous materials*; 2004.
- (33) Gale, J. D.; Shah, R.; Payne, M. C.; Stich, I.; Terakura, K. *Catal. Today* **1999**, 50 (3–4), 525–532.
- (34) Metz, S.; Kästner, J.; Sokol, A. A.; Keal, T. W.; Sherwood, P. *Wiley Interdiscip. Rev. Comput. Mol. Sci.* **2014**, 4 (2), 101–110.
- (35) To, J.; Sokol, A. A.; French, S. A.; Catlow, C. R. A.; Sherwood, P.; Van Dam, H. J. J. *Angew. Chemie - Int. Ed.* **2006**, 45 (10), 1633–1638.
- (36) Piccini, G.; Alessio, M.; Sauer, J. *Angew. Chemie - Int. Ed.* **2016**, 55 (17), 5235–5237.

- (37) Artioli, G.; Lamberti, C.; Marra, G. L. *Acta Crystallogr. Sect. B Struct. Sci.* **2000**, *56* (1), 2–10.
- (38) J.A. Hriljac, M. M. Eddy, J. A. Donohue, G. J. Ray, A. K. C. *J. Solid State Chem.* **1993**, *106* (1), 66–72.
- (39) Sastre, G.; Fornes, V.; Corma, A. *J. Phys. Chem. B* **2002**, *106* (3), 701–708.
- (40) Ghorbanpour, A.; Rimer, J. D.; Grabow, L. C. *Catal. Commun.* **2014**, *52*, 98–102.
- (41) Sherwood, P.; De Vries, A. H. ; Collins, S. J.; Greatbanks, S. P.; Burton, N. A.; Vincent, M. A.; Hillier, I. H. *Faraday Discuss* **1997**, *106*, 79–92.
- (42) Hill, J. R.; Sauer, J. *J. Phys. Chem.* **1994**, *98* (4), 1238–1244.
- (43) Hill, J.-R.; Sauer, J. *J. Phys. Chem.* **1995**, *99* (23), 9536–9550.
- (44) Keal, T. W.; Tozer, D. J. *J. Chem. Phys.* **2005**, *123* (12).
- (45) Guest, M. F.; Bush, I. J.; Van Dam, H. J.; Sherwood, P.; Thomas, J. M. H.; Van Lenthe, J. H.; Havenith, R. W.; Kendrick, J. *Mol. Phys.* **2005**, *103* (6–8), 719–747.
- (46) Grimme, S. *J. Comput. Chem.* **2006**, *27* (15), 1787–1799.
- (47) Valiev, M.; Bylaska, E. J.; Govind, N.; Kowalski, K.; Straatsma, T. P.; Van Dam, H. J. J.; Wang, D.; Nieplocha, J.; Apra, E.; Windus, T. L.; De Jong, W. A. *Comput. Phys. Commun.* **2010**, *181* (9), 1477–1489.
- (48) Ahlrichs, R.; Taylor, P. R. *J. Chim. Phys* **1981**, *78*, 315–324.
- (49) Hartree, D. R. *Math. Proc. Cambridge Philos. Soc.* **1928**, *24* (3), 426.

- (50) Fock, V. *Zeitschrift fur Phys.* **1930**, *61* (1–2), 126–148.
- (51) Smith, W.; Yong, C. W.; Rodger, P. M. *Mol. Simul.* **2002**, *28* (May 2015), 37–41.
- (52) Broyden, C. G. *Math. Comput.* **1970**, *24* (110), 365–365.
- (53) Fletcher, R. *Comput. J.* **1970**, *13* (3), 317–322.
- (54) Goldfarb, D. *Math. Comput.* **1970**, *24* (109), 23–23.
- (55) Shanno, D. F. *Math. Comput.* **1970**, *24* (111), 647–647.
- (56) Swope, W. C.; Andersen, H. C.; Berens, P. H.; Wilson, K. R. *J. Chem. Phys.* **1982**, *76* (1), 637–649.
- (57) Kästner, J.; Carr, J. M.; Keal, T. W.; Thiel, W.; Wander, A.; Sherwood, P. *J. Phys. Chem. A* **2009**, *113* (43), 11856–11865.
- (58) Haase, F.; Sauer, J. *J. Am. Chem. Soc.* **1995**, *117* (13), 3780–3789.
- (59) Kotrla, J.; Nachtigallova, D.; Kubelková, L.; Heeribout, L.; Doremieux-Morin, C.; Fraissard, J. *J. Phys. Chem. B* **1998**, *102* (14), 2454–2463.
- (60) Goodrow, A.; Bell, A. T. *J. Phys. Chem. C* **2008**, *112* (34), 13204–13214.
- (61) Hemelsoet, K.; Ghysels, A.; Mores, D.; De Wispelaere, K.; Van Speybroeck, V.; Weckhuysen, B. M.; Waroquier, M. *Catal. Today* **2011**, *177* (1), 12–24.
- (62) van Duijneveldt, F. B.; van de Rijdt, J. G. C. M. va. D.; van Lenthe, J. H. *Chem. Rev.* **1994**, *94* (7), 1873–1885.
- (63) Svelle, S.; Tuma, C.; Rozanska, X.; Kerber, T.; Sauer, J. *J. Am. Chem. Soc.* **2009**, *131* (2),

816–825.

- (64) Omojola, T.; Cherkasov, N.; McNab, A. I.; Lukyanov, D. B.; Anderson, J. A.; Rebrov, E. V.; van Veen, A. C. *Catal. Letters* **2018**, *148* (1), 474–488.
- (65) Pope, C. G. *J. Chem. Soc. Faraday Trans.* **1993**, *89* (7), 1139–1141.
- (66) Lee, C.-C.; Gorte, R. J.; Farneth, W. E. *J. Phys. Chem. B* **1997**, *101* (19), 3811–3817.
- (67) Blaszkowski, S. R.; van Santen, R. A. *J. Phys. Chem.* **1995**, *99*, 11728–11738.
- (68) Blaszkowski, S. R.; Van Santen, R. A. *J. Am. Chem. Soc.* **1996**, *118* (21), 5152–5153.
- (69) Blaszkowski, S. R.; van Santen, R. A. *J. Phys. Chem.* **1995**, *99* (30), 11728–11738.
- (70) Štich, I.; Gale, J. D.; Terakura, K.; Payne, M. C. *J. Am. Chem. Soc.* **1999**, *121* (14), 3292–3302.
- (71) Plant, D. F.; Simperler, A.; Bell, R. G. *J. Phys. Chem. B* **2006**, *110* (12), 6170–6178.
- (72) Gu, Y.; Kar, T.; Scheiner, S. *J. Am. Chem. Soc.* **1999**, *121* (40), 9411–9422.
- (73) Kumara Swamy, K. C.; Kumaraswamy, S.; Kommana, P. *J. Am. Chem. Soc.* **2001**, *123* (50), 12642–12649.
- (74) Koller, H.; Engelhardt, G.; van Santen, R. A. *Top. Catal.* **1999**, *9* (3–4), 163–180.
- (75) Hunger, M.; Horvath, T. *J. Am. Chem. Soc.* **1996**, *118* (49), 12302–12308.
- (76) Zecchina, A.; Bordiga, S.; Spoto, G.; Scarano, D.; Spanò, G.; Geobaldo, F. *J. Chem. Soc. - Faraday Trans.* **1996**, *92* (23), 4863–4875.

- (77) Anderson, M. W.; Barrie, P. J.; Klinowski, J. *J. Phys. Chem* **1991**, *95*, 235–239.
- (78) De Wispelaere, K.; Wondergem, C. S.; Ensing, B.; Hemelsoet, K.; Meijer, E. J.; Weckhuysen, B. M.; Van Speybroeck, V.; Ruiz-Martínez, J. *ACS Catal.* **2016**, *6* (3), 1991–2002.
- (79) Hwang, A.; Kumar, M.; Rimer, J. D.; Bhan, A. *J. Catal.* **2017**, *346*, 154–160.
- (80) Shah, R.; Gale, J. D.; Payne, M. C. *J. Phys. Chem.* **1996**, *100* (96), 11688–11697.
- (81) Izmailova, S. G.; Karetina, I. V.; Khvoshchev, S. S.; Shubaeva, M. A. *J. Colloid Interface Sci.* **1994**, *165* (2), 318–324.
- (82) von Ballmon, R.; Higgins, J. B.; Treacy, M. M. J. *Proc. from Ninth Int. Zeolite Conf.* **1993**, *2*, 255.
- (83) Nguyen, C. M.; Reyniers, M. F.; Marin, G. B. *Phys. Chem. Chem. Phys.* **2010**, *12* (32), 9481–9493.
- (84) Nusterer, E.; Blöchl, P. E.; Schwarz, K. *Angew. Chemie (International Ed. English)* **1996**, *35* (2), 175–177.